Proceedings of the
Annual Stability Conference
Structural Stability Research Council
Nashville, Tennessee, March 24-27, 2015

Observations from Cyclic Tests on Deep, Slender Wide-Flange Structural Steel Beam-Column Members

Chia-Ming Uang[1], Gulen Ozkula[2], John Harris[3]

Abstract
As part of a National Institute of Standards and Technology (NIST) comprehensive research program to study the seismic behavior and design of deep, slender wide-flange structural steel beam-column members for application in seismic design and construction of steel Special Moment Frames (SMF), twenty-five deep column specimens were subjected to inelastic cyclic loading with three different levels of constant axial load. The test matrix included five W24 sections (W24×55 to W24×176) in order to cover a wide range of element slenderness ratios for flange local buckling and web local buckling; the lighter sections also widened the member slenderness ratio for lateral-torsional buckling and weak-axis flexural buckling. Three levels of constant axial load (C_a = 0.2, 0.4, and 0.6) were used in the test program. All specimens were subjected to strong-axis bending except for three specimens that were subjected to weak-axis bending and one specimen that was subjected to biaxial bending. Test results showed that the slenderness ratios had a significant effect on the failure mode—local versus global buckling. The presence of an axial load produced significant local buckling and axial shortening. The level of axial load also affected the plastic rotation capacity. Specimens with weak-axis bending were ductile, showing no local buckling up to a high drift level. Most of the strong-axis bending specimens were not able to deliver a plastic rotation of 0.03 radians.

1. Introduction

Research on the cyclic behavior of W14 columns under high axial load and seismic drift for braced frame applications has been conducted by Newell and Uang (2008). For SMF design, however, designers prefer to use deeper columns (e.g., W24 to W36 sections) to satisfy code-enforced story drift limits. Since the slenderness ratios for both local buckling and global buckling are significantly higher for deep columns, they are prone to various forms of buckling that may impair their gravity load-carrying capacity. Unfortunately, little experimental research is available to support the seismic design or assessment provisions in AISC 341 (AISC 2010a) and ASCE 41 (ASCE 2013). To fill this gap, NIST developed a comprehensive research plan to study the seismic behavior and design of deep, slender wide-flange structural steel beam-column members (NIST 2011). The plan included studies at the member, subassemblage, and system levels. The first step

[1] Professor, University of California San Diego, < cmu@ucsd.edu >
[2] Graduate Research Assistant,, University of California San Diego, < gozkula@ucsd.edu >
[3] Research Structural Engineer, National Institute of Standards and Technology, < john.harris@nist.gov >

in implementing this plan was to evaluate experimentally the cyclic behavior of deep columns. Test results will then be used by NIST to validate computational models and to improve seismic design provisions.

2. Test Setup and Specimens

Twenty-five W24 specimens were subjected to three different levels of constant axial load combined with cyclic story drift demands; see Table 1 for the text matrix. A total of five wide-flange sections were selected in order to cover a wide range of element slenderness ratios for flange local buckling (FLB) and web local buckling (WLB); the use of lighter sections (W24×84 and W24×55) also widened the range of member slenderness ratios for lateral-torsional bucking (LTB). Figure 1 shows a comparison of the flange and web width-to-thickness ratios with the seismically compact limits prescribed in AISC 341. The limiting width-to-thickness ratios for highly ductile (λ_{hd}) and moderately ductile (λ_{md}) elements are also shown in Fig. 1, where for FLB,

$$\lambda_{hd} = 0.3\sqrt{E/F_y} \tag{1}$$

and for WLB when C_a ($= P/\phi_c P_y$) larger than 0.125,

$$\lambda_{hd} = 0.77\sqrt{E/F_y}\,(2.93 - C_a) \geq 1.49\sqrt{E/F_y} \tag{2}$$

In **Table 1**, the unbraced length, L, is also normalized by

$$L_{hd} = 0.086\, r_y\, E/F_y \tag{3}$$

Note that L_{hd} is the limiting unbraced length for beams in AISC 341, but not columns, in an SMF. In the specimen designation, "L", "M", and "H" represent low (C_a=0.2), medium (C_a=0.4), and high (C_a=0.6) axial load levels, respectively. Only one specimen (2Z) was tested without any axial load. Two specimens (2L-P and 6L-P) were tested monotonically, one for strong-axis and the other one for weak-axis bending. Specimen 7M was tested with bi-axial bending, and Specimen 8M was tested by using a near-field loading protocol. Each specimen was 18 feet long with 3 inch base plates welded at each end. ASTM A992 steel was specified for the specimens. The material properties obtained from tensile coupon tests are summarized in Table 2.

The overall geometry of the test setup is shown in Fig. 2. Testing was conducted in the Seismic Response Modification Device (SRMD) Test Facility at the University of California, San Diego. As shown in Fig. 2, beam-column specimens were tested in a horizontal position with one end attached to a strong wall fixture while the other end was attached to a reaction block on the shake table. All specimens were tested with fixed-fixed boundary conditions. For a typical test, the target axial load was first applied to the specimen and held constant. Then a pseudo-static cyclic displacement history was applied to one end; the AISC loading protocol for testing steel moment connections was used for this purpose—see AISC 341 (AISC 2010a).

Table 1: Test Matrix

Group No.	Shape	Specimen Designation	Normalized Slenderness			Column Axial Load		Bending Direction
			$\frac{(b_f/2t_f)}{\lambda_{hd}}$	$\frac{(h/t_w)}{\lambda_{hd}}$	$\frac{L}{L_{hd}}$	C_a	P (kips)	
1	W24×176	1L	0.67	0.57	1.42	0.2	465	Strong-Axis
		1M		0.61		0.4	931	
		1H		0.66		0.6	1396	
2	W24×131	2Z	0.93	0.66	1.46	0.0	0	
		2L		0.70		0.2	347	
		2L-P		0.70		0.2	347	
		2M		0.76		0.4	693	
		2H		0.82		0.6	1040	
3	W24×104	3L	1.18	0.85	1.49	0.2	276	
		3M		0.91		0.4	551	
		3H		1.00		0.6	826	
4	W24×84	4L	0.81	0.91	2.22	0.2	222	
		4M		0.98		0.4	445	
5	W24×55	5L	0.81	1.08	3.23	0.2	146	
		5LM		1.12		0.3	219	
		5M		1.26		0.4	292	
6	W24×131	6L	0.93	0.70	1.46	0.2	347	Weak Axis
		6L-P		0.70		0.2	1040	
		6H		0.82		0.6	1040	
7	W24×131	7M	0.93	0.76	1.46	0.4	693	Biaxial-Axis
8	W24×131	8M	0.93	0.76	1.46	0.4	693	Strong Axis, Near Field

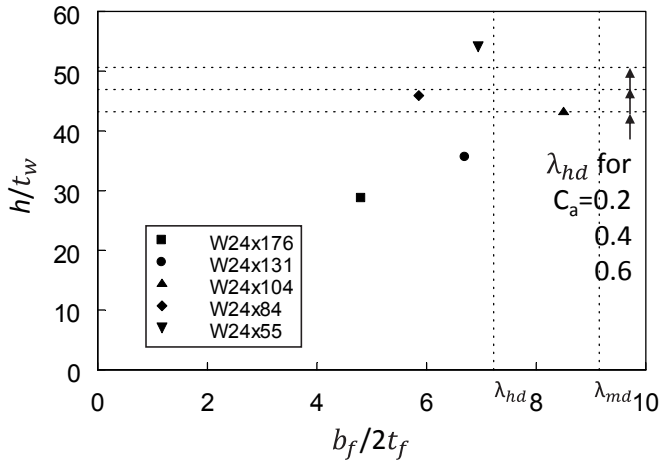

Figure 1 Comparison of width-to-thickness ratios

Table 2: Tensile Coupon Test Results

Shape	Component	Yield Stress (ksi)	Tensile Strength (ksi)	Elongation (%)
W24×176	Flange	52.5	81.8	38.1
	Web	58.5	82.5	38.0
W24×131	Flange	50.8	75.9	38.4
	Web	55.4	77.7	35.4
W24×104	Flange	51.5	78.0	36.5
	Web	58.1	80.6	31.3
W24×84	Flange	51.3	77.6	36.2
	Web	58.8	80.2	31.0
W24×55	Flange	53.7	71.5	38.0
	Web	59.8	74.3	32.4

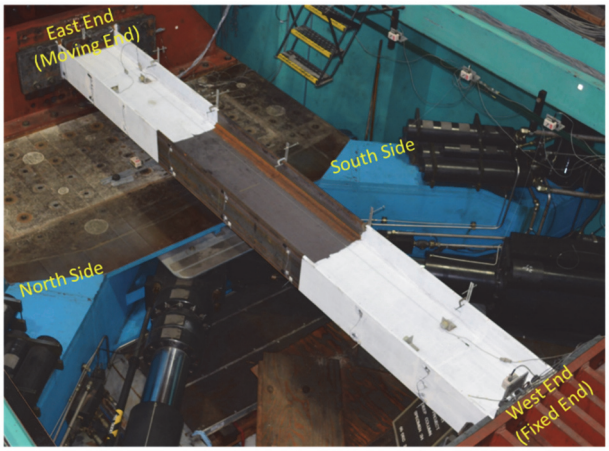

Figure 2 Test Setup

3. Data Reduction

In the following presentation, the story drift ratio (SDR) is defined as the imposed lateral displacement, Δ, divided by the column length, H. Assuming an inflection point at mid-height of the column, the end moment can be computed as

$$M = \frac{1}{2}(VH - P\Delta) \tag{4}$$

where V is the measured lateral load (i.e., column shear) and P is the measured axial load. End moment can be normalized by either the plastic moment, M_p, or the reduced plastic moment, M_{pc}:

$$M_{pc} = 1.18\left(1 - \frac{P}{P_y}\right)M_p \leq M_p \tag{5}$$

The measured yield stresses were used to compute these strengths.

4. Experimental Results

4.1 Group 2: W24×131 Specimens

Group 2 served as the reference group for comparison with the response of the other groups. The response of five specimens (2Z, 2L, 2L-P, 2M, and 2H) is presented first. To evaluate the effect of axial load, 2Z without an axial load was included in this group. This "beam" specimen was able

to reach 7% drift without any strength degradation before one flange fractured near the weld access hole. Local buckling was minimal. By applying and increasing the level of axial force for the remaining three specimens, local buckling at member ends became more significant. Figure 3 shows that increasing the axial force level reduced the maximum flexural strength, triggered earlier local buckling, accelerated strength degradation in the post-yield region, as well as reduced the energy dissipation and deformation capacities. For example, local buckling was visible during 3% drift cycles for Specimen 2L (C_a=0.2), but local buckling was visible for Specimen 2H (C_a=0.6) at 0.75% drift cycles. Between the local buckling regions, the specimens remained essentially straight and showed no sign of out-of-plane global buckling (either flexural buckling or lateral-torsional buckling).

Specimen 2L was cyclically tested up to 4% drift only. To evaluate the axial capacity of a flexurally-yielded column, after unloading the lateral load, the specimen was axially compressed in its residual position to axial failure. The specimen eventually experienced out-of-plane flexural buckling with a buckling strength of 1500 kips. Assuming an effective length factor of 1.0 and using a member length equal to the distance between two severely buckled regions (=187 in.), the computed strength per AISC 360 (AISC 2010b) was 1465 kips, which correlated well with the measured value. To evaluate the cyclic loading effect, one extra specimen, 2L-P, was monotonically loaded to 4% drift, and this "pushover" response is compared with the Specimen 2L backbone curve in Fig. 12.

4.2 Group 1: W24×176 Specimens

This group is more compact than Group 2. Therefore, the slenderness ratios for both local buckling and LTB were smaller (see Table 1). It was expected that more ductility could be developed from these specimens and the extent of local buckling was less. However, testing showed that, unexpectedly, LTB was the dominant failure mode (see Fig. 6).

It was shown that Specimen 2L started to show local buckling at 3% drift. The stockier section of Specimen 1L delayed it to 4% drift (see Fig. 4). Note that the yielded length of this group of specimens was much longer when compared with those of the other groups. By having a more compact section, the onset of local buckling was delayed and it allowed more significant strain hardening to occur; see Table 3 for the cyclic stain hardening ratios (M_{max}/M_{pc}). The larger moment developed at the column ends resulted in a longer yielded length (see Fig. 5). Therefore, the column was more prone to LTB.

By doubling the axial load for Specimen 1M, local buckling started earlier at 2% drift; the local buckling patterns were antisymmetric at both ends of the column. But long yielded zones at the column ends triggered the same LTB mode like Specimen 1L.

Tripling the axial load for Specimen 1H produced local buckling at 1% drift, and the local buckling pattern at both ends was identical (i.e., symmetric). Long yielded lengths also triggered LTB, but high axial load together with the symmetric local buckling pattern caused the column to experience

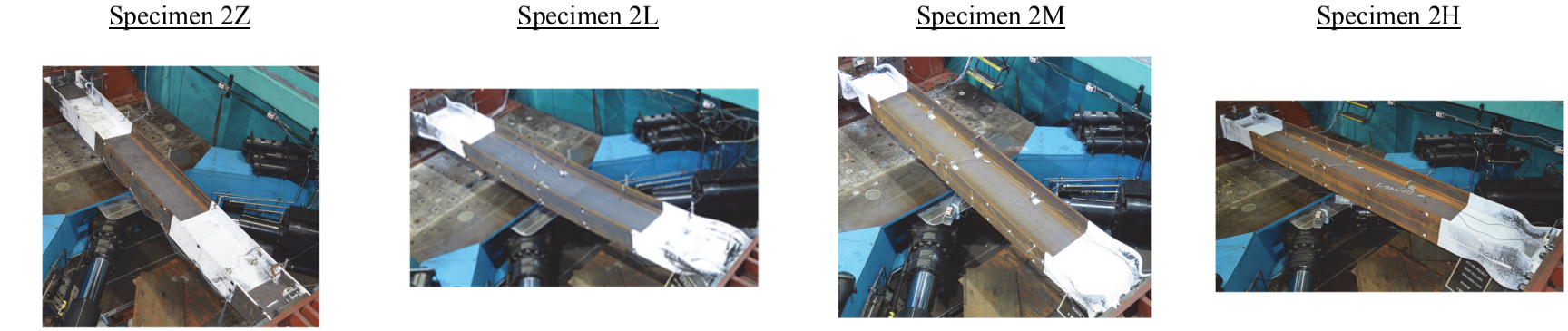

(a) Deformed Configuration

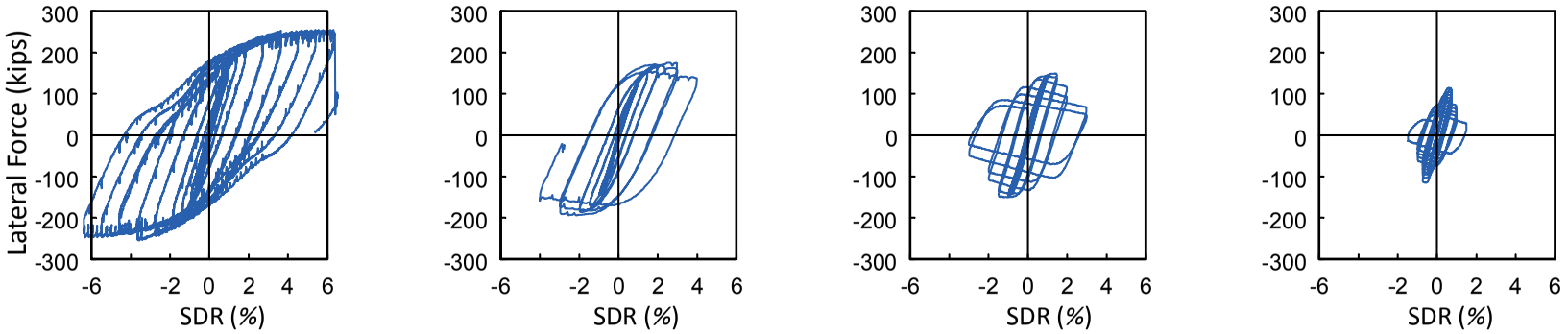

(b) Lateral Load vs. Story Drift Ratio

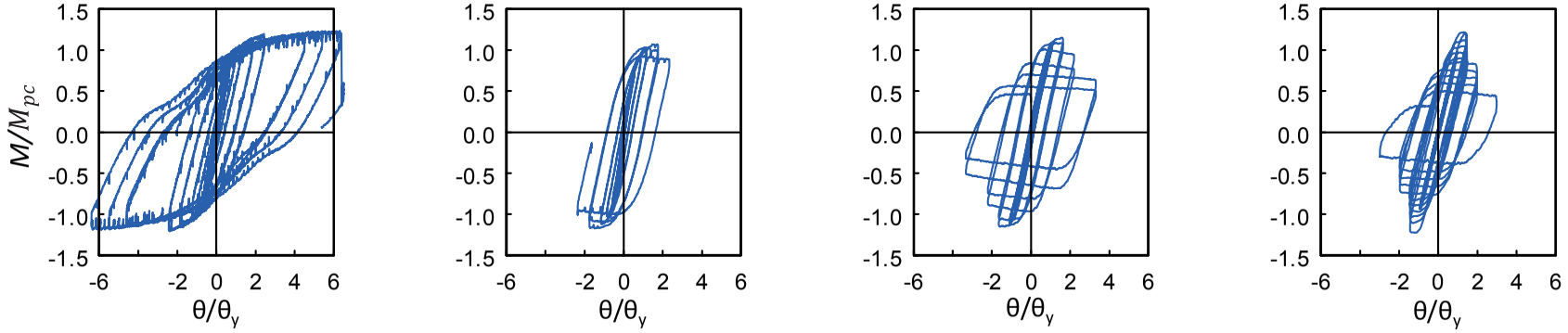

(c) Normalized End Moment vs. Normalized Story Drift

Figure 3 Group 2 (W24×131 Section): Failure Modes and Hysteresis Responses

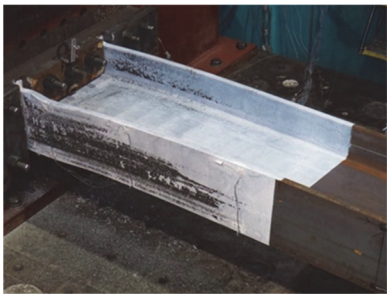

(a) Yielding and Buckling Pattern at -4% Drift

(b) West End

(c) East End

Figure 4 Specimen 1L: Deformation at Column Ends (7% Drift)

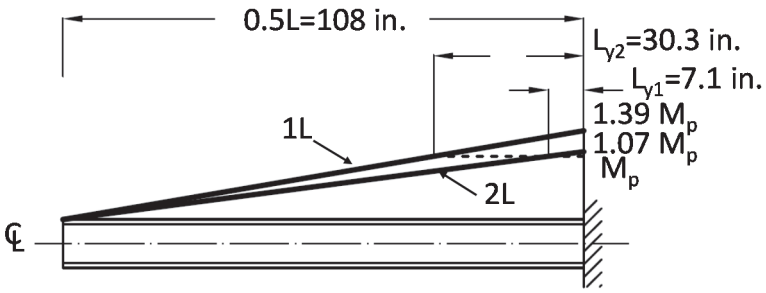

Figure 5 Comparison of Yielded Length

flexural buckling. In summary, all three Group 1 specimens first showed local buckling, but eventually failed in global buckling. The yielding lengths were the longest among all groups tested in this test program due to the much stockier section used. Specimen 1H showed single-curvature flexural buckling, probably because the local buckling patterns at both ends was symmetric. Specimens 1L and 1M had antisymmetric local buckling patterns, and both failed in an S-shaped (double-curvature) LTB mode. Figure 6 shows the failure mode and hysteresis response of all three specimens.

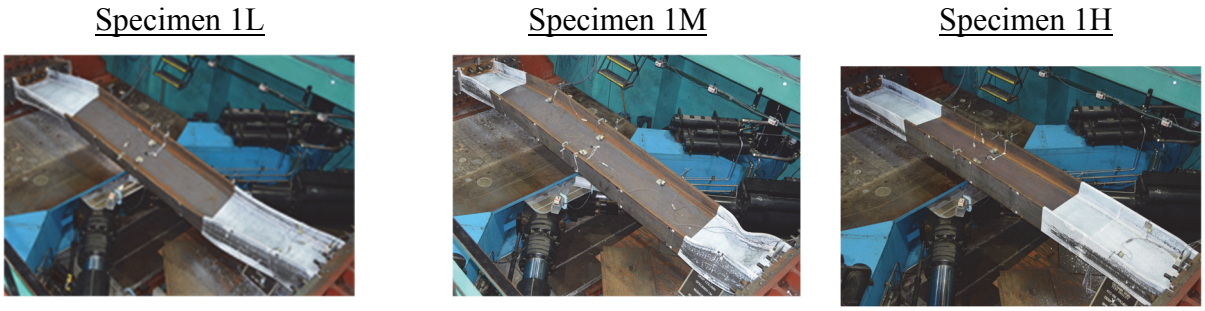

(a) Deformed Configuration

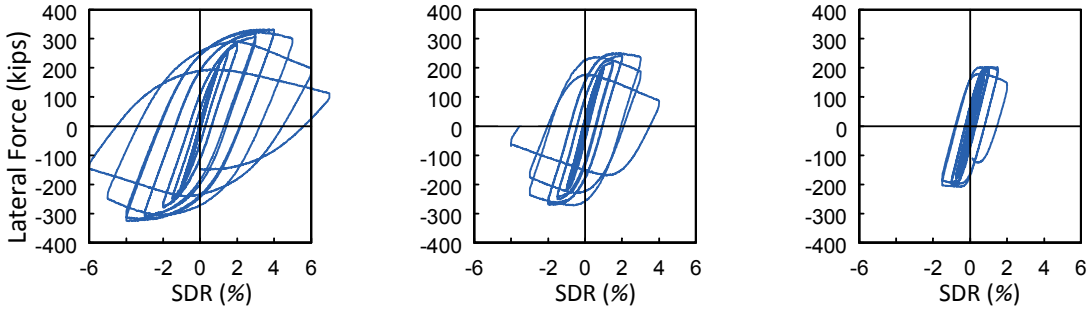

(b) Lateral Load vs. Story Drift Ratio

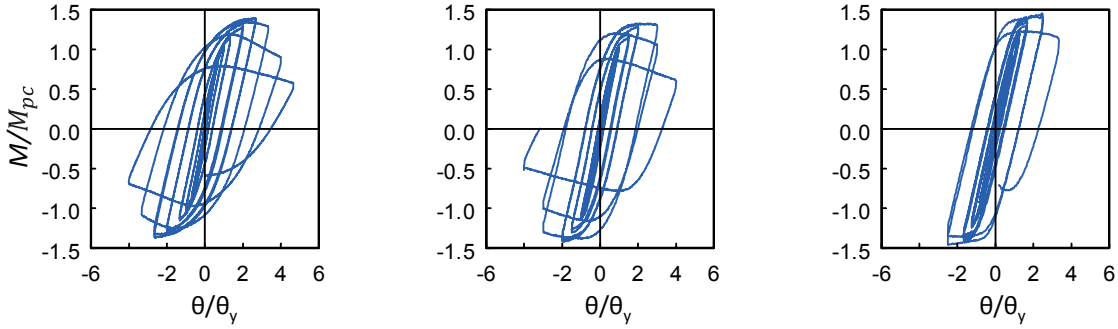

(c) Normalized End Moment vs. Normalized Story Drift

Figure 6 Group 1 (W24×176 Section): Failure Modes and Hysteresis Responses

4.3 Group 3: W24×104 Specimens

The web of Group 3 specimens was classified as highly ductile, but the flanges only satisfied the moderately ductile requirement. All three specimens experienced FLB first, which then *interacted* with WLB. Significant local buckling occurred at high drift levels or when the axial load was high, which was accompanied by considerable column shortenings. No global buckling was observed. Depending on the direction of local buckling at member ends, one end at the buckled region might move out-of-plane in one direction, while the other end moved in either the same or opposite direction, thus causing the column in between to twist as a rigid body motion slightly. But such deformation had nothing to do with global buckling. Figure 7 summarizes the failure mode and hysteresis response of all three specimens.

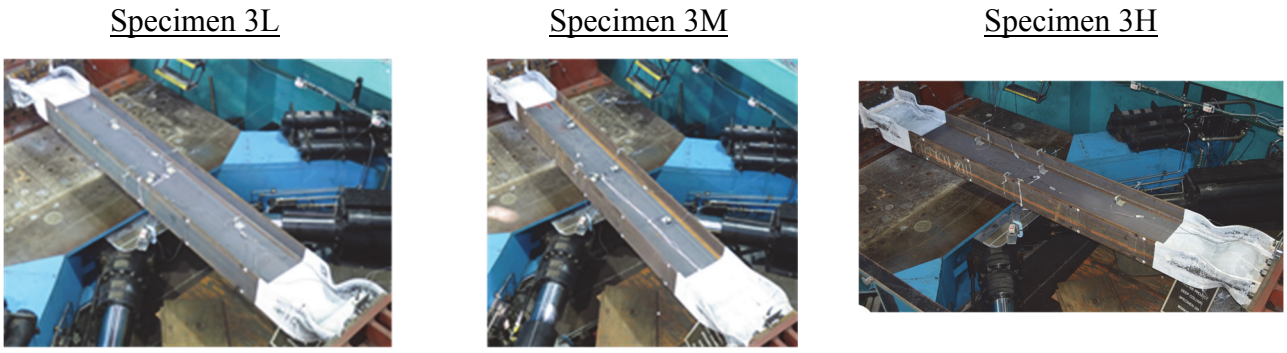

(a) Deformed Configuration

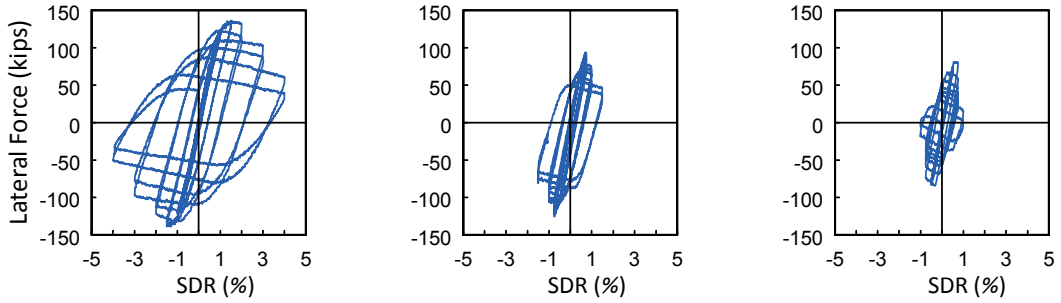

(b) Lateral Load vs. Story Drift Ratio

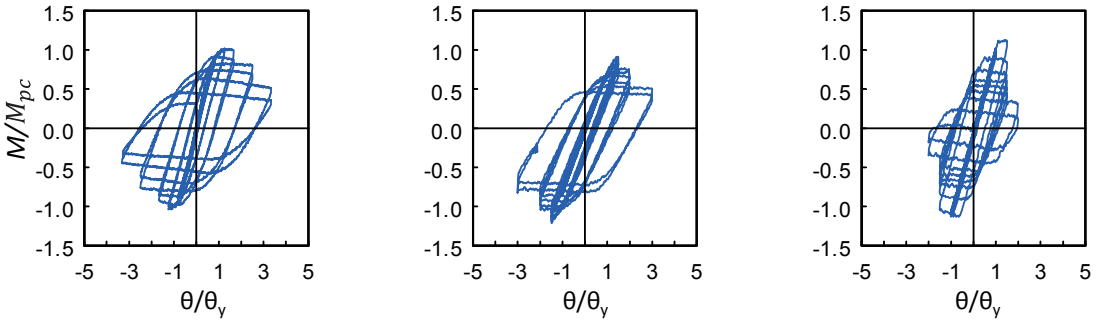

(c) Normalized End Moment vs. Normalized Story Drift

Figure 7 Group 3 (W24×104 Section): Failure Modes and Hysteresis Responses

4.4 Group 4: W24×84 Specimens

The flange of the Group 4 specimens was classified as highly ductile, and the web had width-thickness ratios in the neighborhood of λ_{hd}. One specimen (4L) with C_a=0.2 experienced brittle fracture near the weld access hole at 2% drift. It was decided not to test the specimen originally planned for high axial load (4H) so that testing of 4L could be repeated. Although the slenderness ratio for LTB of this group of specimens was about 50% higher than those of the first three groups, both specimens did not fail in LTB or flexural buckling. Instead, local buckling dominated the responses. Compared to Groups 1 and 2 specimens, the larger width-to-thickness ratio of the web caused them to buckle along the entire depth of the web, which in turn triggered local buckling of both flanges at each end. The direction of local buckling was opposite at both ends. Therefore,

(a) Deformed Configuration

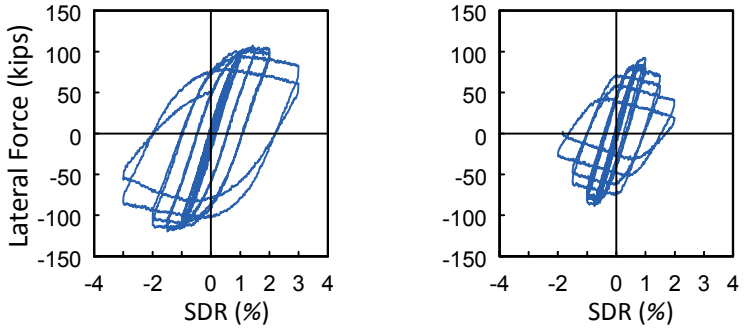

(b) Lateral Load vs. Story Drift Ratio

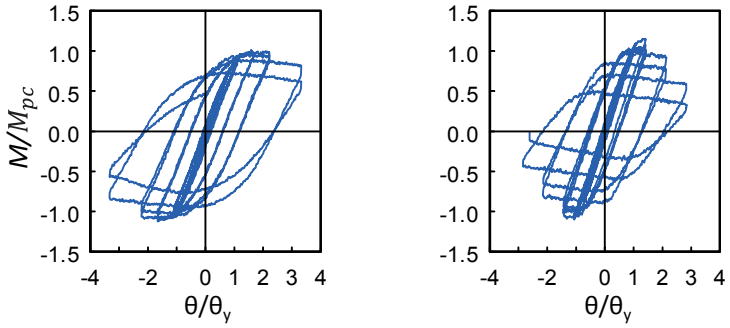

(c) Normalized End Moment vs. Normalized Story Drift

Figure 8 Group 4 (W24×84 Section): Failure Modes and Hysteresis Responses

both specimens failed in double-curvature configuration. Because local buckling developed along the full section depth, axial shortening was significant.

4.5 Group 5: W24×55 Specimens

Three specimens were planned for this group. After testing 5L (C_a=0.2) and 5M (C_a=0.4), it was observed that the measured ductility capacity was limited. Instead of testing the last specimen (5LM) at the high axial load (C_a=0.6), it was decided to test it with an intermediate C_a value of 0.3; the specimen was designated as 5LM. The slenderness ratio for LTB was 2.2 times that of the Group 2 specimens. The flanges were highly ductile, but the web did not meet the highly ductile requirement. Specimen 5L was below, 5LM was practically at, and 5M exceeded the limiting value for a moderately ductile web.

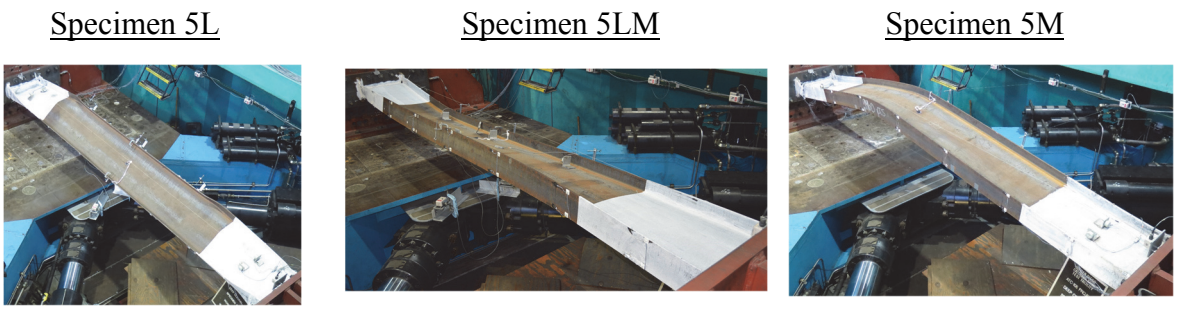

(a) Deformed Configuration

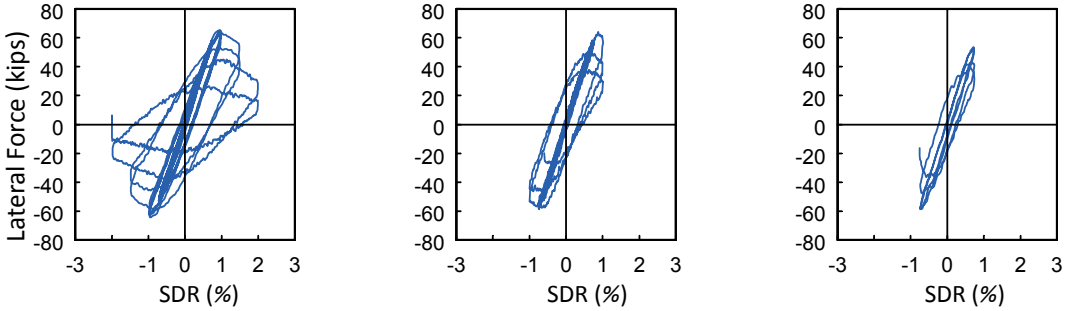

(b) Lateral Load vs. Story Drift Ratio

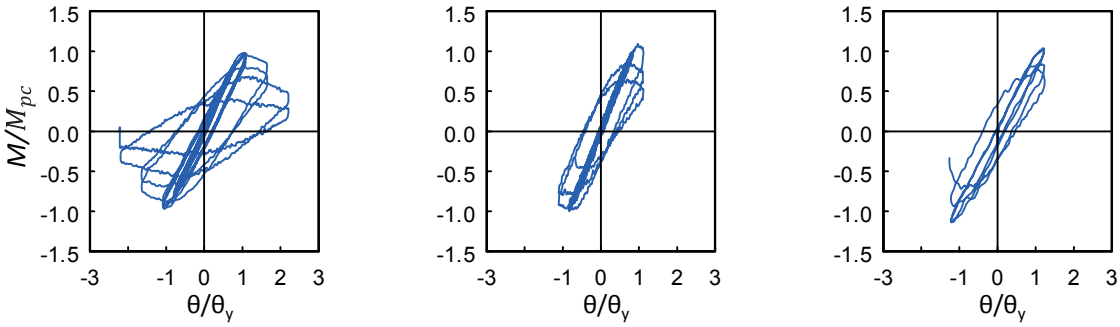

(c) Normalized End Moment vs. Normalized Story Drift

Figure 9 Group 5 (W24×55 Section): Failure Modes and Hysteresis Responses

With little sign of local buckling, Specimen 5L experienced LTB during the 1.5% drift cycles. Alternating loading caused the same (south) flange to buckle in the same (upward) direction. The deformation amplitude was significant at 2% drift before the test was stopped. Figure 9 shows that LTB caused the middle portion of the column to tilt about its longitudinal axis. Local buckling was observed at one end, but it was triggered by LTB. Specimens 5LM and 5M also showed LTB first at lower drift levels. But Specimen 5M turned to flexural buckling about the weak-axis buckling during the fourth negative excursion to 0.75% drift. Specimen 5LM also turned to the same flexural buckling mode, but at a slightly higher (1%) drift level. The failure mode and hysteresis response are summarized in Fig. 9.

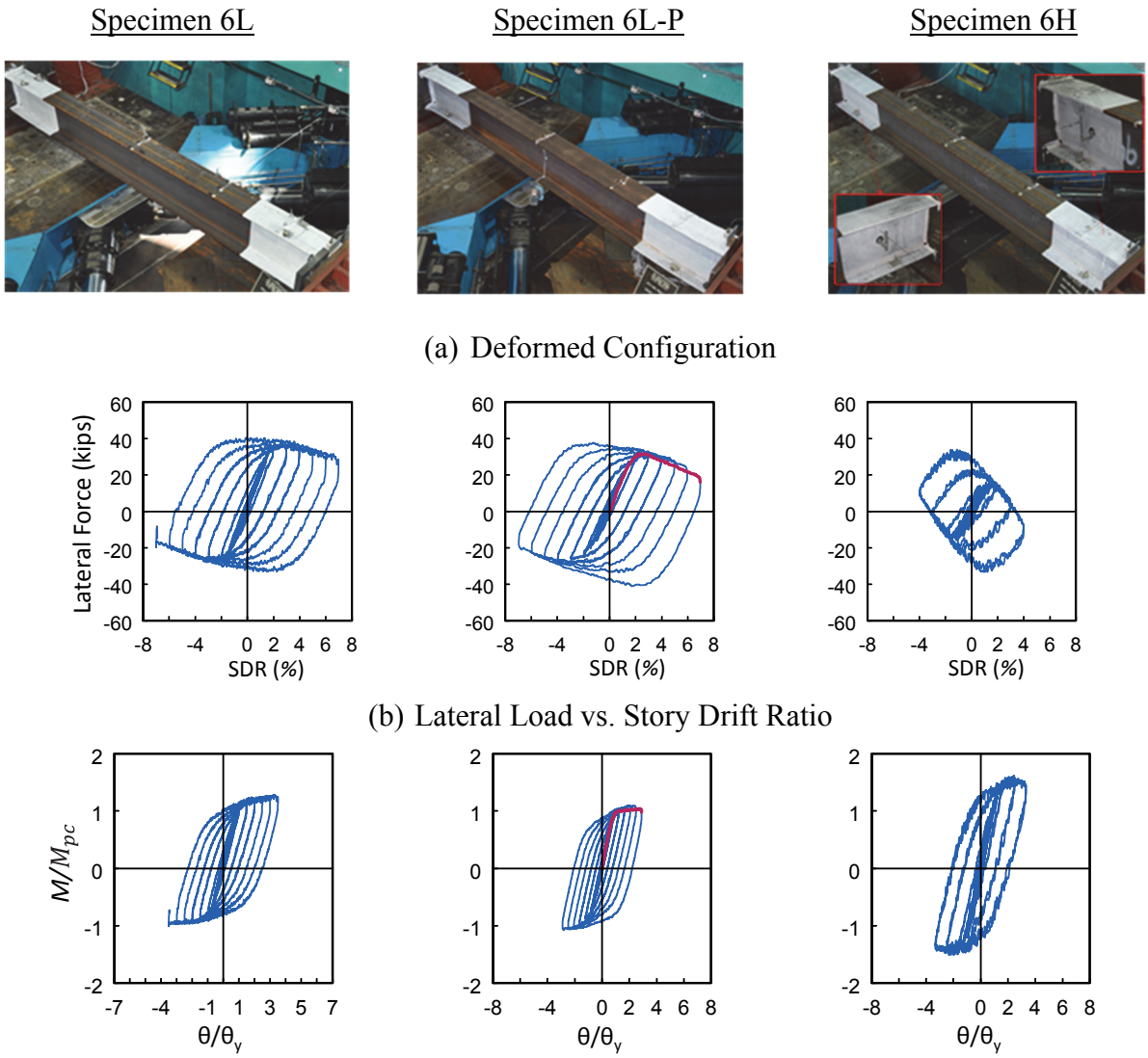

Figure 10 Group 6 (W24×131 Section): Failure Modes and Hysteresis Responses

3.6 Group 6: W24×131 Specimens

Groups 6 and 2 specimens had the same shape and material properties, except that the former specimens were subjected to weak-axis bending. Specimen 6L was loaded to 7% drift. As expected, LTB was not a concern for weak-axis bending. It is also interesting to note that neither

WLB nor FLB was observed, and the specimen performed in a ductile manner. Upon unloading the lateral load, it was decided to monotonically compress the column in order to evaluate the residual axial load capacity. The specimen failed by weak-axis flexural buckling.

After observing the stable response of Specimen 6L, it was decided to test Specimen 6H. Under high axial load, minor web and flange buckling at both ends developed. The test was stopped at 4% drift due to the *P*-Δ effect, the restoring force practically diminished at this drift level.

To evaluate the cyclic loading effect, it was then decided to laterally load the third specimen (6L-P) to 7% drift in order to generate a monotonic response for comparison with the backbone curve of Specimen 6L. Thereafter, the specimen was subjected to the AISC loading protocol in a reverse order from 7% drift to evaluate the loading sequence effect. As shown in Fig. 10, the sequence of loading did not affect the failure mode nor the strength of the column. But the post-buckling negative stiffness was reduced somewhat when the AISC loading protocol was applied in a reverse order.

5. Analysis of Test Results

5.1 Backbone Curves and Overstrength

Backbone curve of each cyclically loaded specimen was derived from the first cycle of each story drift level (see procedure prescribed in ASCE 2013) as shown in Fig. 11(a). The backbone curves of each of the six groups in Fig. 12 show that the level of axial load significantly affected both the strength and plastic rotation capacity of the columns.

It was observed from the behavior of Group 1 specimens (Section 3.2) that significant strain hardening could alter the failure mode and trigger global buckling mode. The strain hardening ratio is evaluated as the ratio between the maximum end moment and the reduced plastic moment, M_{pc}, in Eq. (5). The ratios thus computed are listed in Table 3.

Table 3: Member Overstrength and Rotational Capacity

Specimen	M_{max} (kip-ft)	M_{max}/M_{pc}	θ_{yc} (×0.01 rad)	θ_p (×0.01 rad)	R_p
1L	3148	1.4	1.5	3.7	2.5
1M	2423	1.3	1.0	2.3	2.3
1H	2010	1.5	0.6	1.2	2.0
2Z	2327	1.5	1.5	6.5	4.3
2L	1655	1.1	1.7	2.0	1.2
2M	1430	1.2	0.9	1.0	1.1
2H	1084	1.2	0.5	0.4	0.8
3L	1262	1.0	1.2	1.4	1.2
3M	880	0.9	0.7	0.4	1.0
3H	779	1.1	0.5	0.4	0.8
4L	1039	1.1	0.9	1.5	1.7
4M	897	1.2	0.7	0.7	1.0
5L	599	1.0	0.9	0.6	0.7
5LM	594	1.1	0.9	0.2	0.2
5M	494	1.1	0.6	NA	NA
6L	454	1.3	2.0	5.6	2.8
6L-P	406	1.1	2.4	4.8	2.0
6H	337	1.6	1.2	2.8	2.3

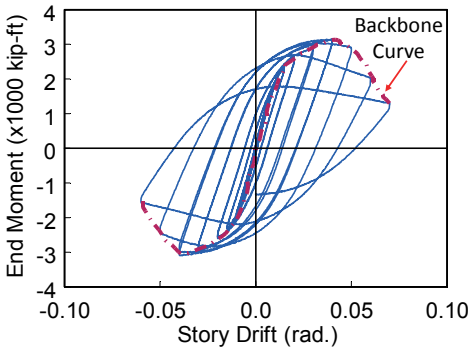

(a) Backbone Curve

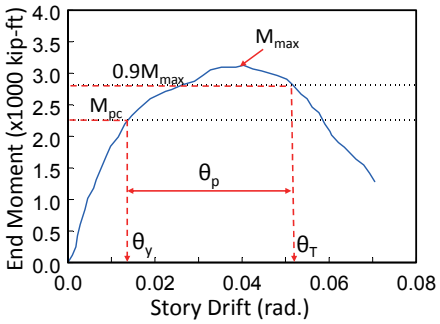

(b) Rotation Capacity

Figure 11 Definition of Backbone Curve and Rotation Capacity

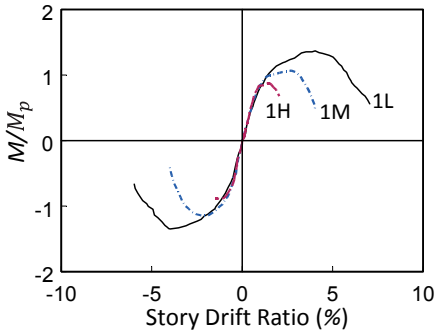

(a) Group 1: W24×176 Section

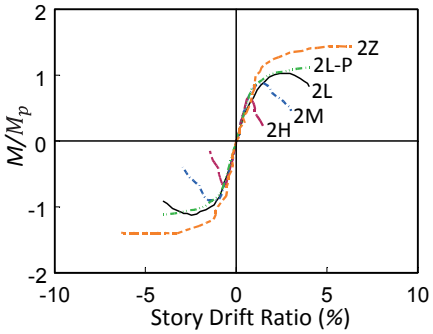

(b) Group 2: W24×131 Section

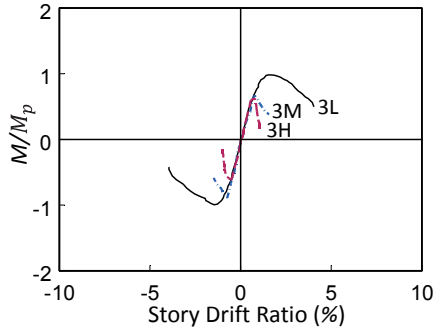

(c) Group 3: W24×104 Section

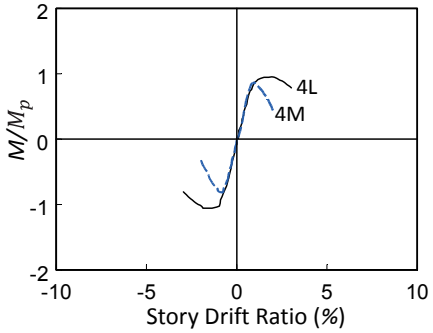

(d) Group 4: W24×84 Section

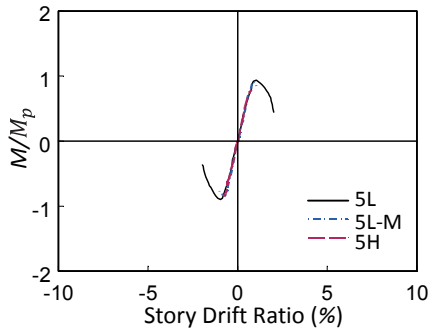

(e) Group 5: W24×55 Section

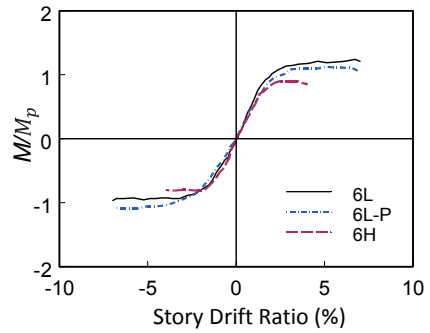

(f) Group 6: W24×131 Section

Figure 12: Comparison of Backbone Curves

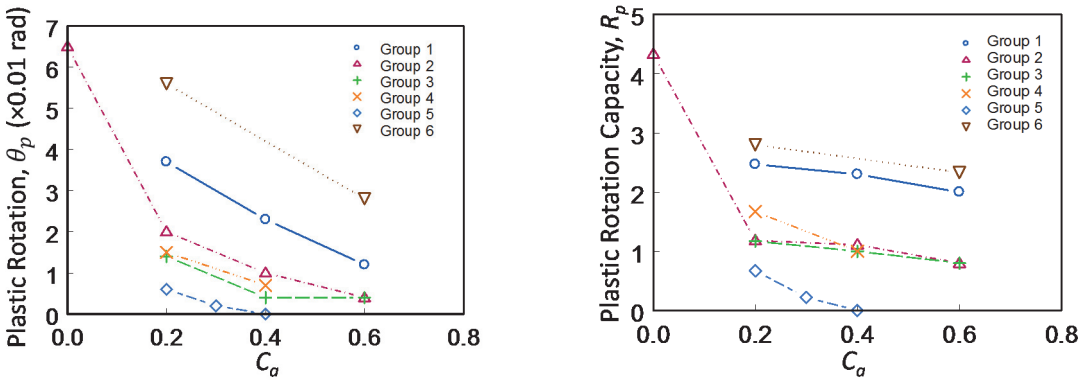

(a) Plastic Rotation vs C_a (b) Plastic Rotation Capacity vs. C_a

Figure 13 Plastic Rotation and Plastic Rotation Capacity

5.2 Plastic Rotation Capacity

Once the backbone curve is constructed, the plastic rotation, θ_p, can be evaluated by the procedure shown in Fig. 10(b). The plastic rotation capacity, R_p, is then computed as

$$R_p = \frac{\theta_T - \theta_y}{\theta_y} = \frac{\theta_p}{\theta_y} \tag{6}$$

Figure 13(a) shows the effect of axial force level on the plastic rotation of six groups of specimens. The weak-axis specimens (Group 6) delivered the highest plastic rotations. Under strong-axis bending, the slenderness ratios for both local and global buckling in addition to axial force level had a significant effect on the plastic rotation. Assuming that an SMF is expected to achieve a story drift of 0.04 radians, taking the elastic component is 0.01 radians, the plastic rotation demand would be 0.03 radians. Fig. 13(a) shows that the majority of deep column specimens failed to deliver this rotation.

5.3 Axial Shortening

With the presence of a constant axial force, most of the column specimens showed significant shortening after severe local buckling or global buckling occurred. The measured shortenings are summarized in Fig. 14. Two plots are presented for each group. The first plot compares the shortenings at the end of each test. To show the effect of axial force level, the second plot compares shortenings at a given drift level; the effect of axial force level is obvious from these plots.

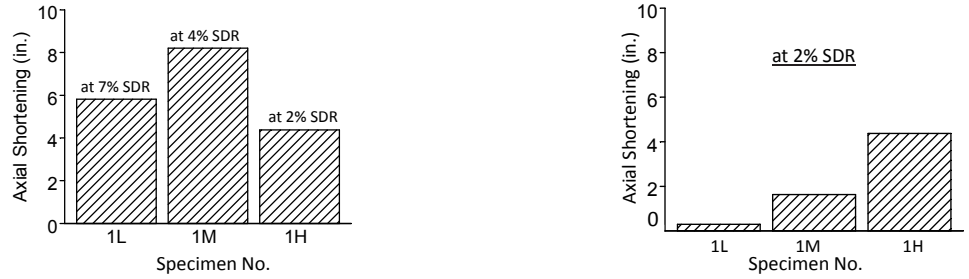

(a) Group 1 (W24×176 Section)

(b) Group 2 (W24×131 Section)

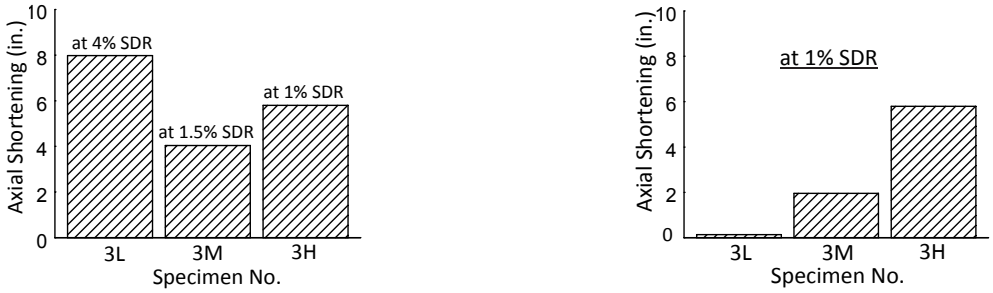

(c) Group 3 (W24×104 Section)

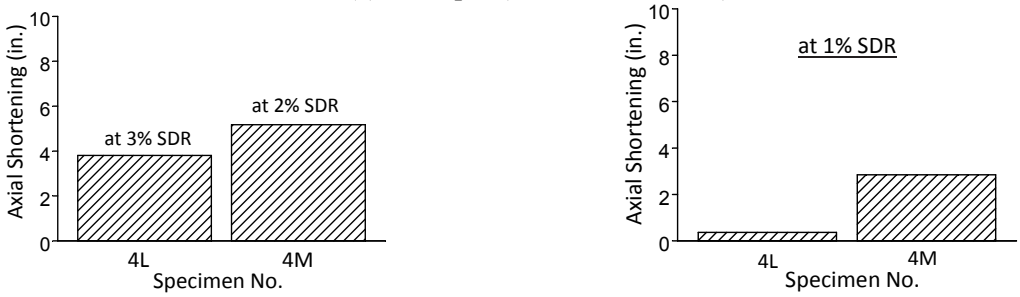

(d) Group 4 (W24×84 Section)

(e) Group 5 (W24×55 Section)

Figure 14 Column Axial Shortening

6. Conclusions

Based on the test results of twenty-five W24 column specimens subjected to cyclic loading with varying levels of constant axial load, the following observations can be made:

(1) The slenderness ratios for local buckling and LTB had a significant effect on the failure mode (local versus global buckling).
(2) The level of axial load affected the plastic rotation capacity. Most of the strong-axis bending specimens were not able to deliver a plastic rotation of 0.03 radians (see Fig. 13).
(3) The presence of an axial load produced significant local buckling and axial shortening (see Fig. 14).
(4) Using a compact section with low width-to-thickness ratios may change the failure mode from local buckling to lateral-torsional buckling (see Fig. 6 for the failure mode of Group 1 specimens). Such change was due to significant strain hardening, which extended the yielded length and triggered lateral-torsional buckling.
(5) Specimens with weak-axis bending were ductile, showing little local buckling up to a very high drift level (see Fig. 10).

7. Acknowledgement

Funding for this research was provided by the NEHRP Consultants Joint Venture under its Earthquake and Structural Engineering Research contract with the National Institute of Standards and Technology. Mr. J.O. Malley from Degenkolb Engineers chaired the Advisory Committee and Mrs. A. Hortacsu from Applied Technology Council served as the Project Manager. The authors also would like to acknowledge the American Institute of Steel Construction for donating steel materials and The Herrick Cooperation for donating fabrication of the test specimens.

References

AISC (2010a). *Seismic Provisions for Structural Steel Buildings*. ANSI/AISC 341-10*,* American Institute of Steel Construction, Chicago, IL.

AISC (2010b). *Specification for Structural Steel Buildings*. ANSI/AISC 360-10*,* American Institute of Steel Construction, Chicago, IL.

ASCE (2013), *Seismic Evaluation and Retrofit of Existing Building Structures*. ASCE/SEI 41-13, American Society of Civil Engineers, Reston, VA.

Newell, J.D. and Uang, C.-M. (2008). "Cyclic Behavior of Steel Wide-Flange Columns Subjected to Large Drift," *Journal of Structural Engineering*, Vol. 134, No. 8, pp. 1334-1342, ASCE.

NIST (2011). *Research Plan for the Study of Seismic Behavior and Design of Deep, Slender, Wide-flange Structural Steel-Beam-Column Members*. NIST-GCR-11-917-13. Produced by the NEHRP Consultants Joint Venture, a partnership of the Applied Technology Council and the Consortium of Universities for Research in Earthquake Engineering, for the National Institute of Standards and Technology, Gaithersburg, MD.